Available online at www.sciencedirect.com
ScienceDirect
International Journal of Heat and Mass Transfer 50 (2007) 566–579
International Journal of HEAT and MASS TRANSFER
www.elsevier.com/locate/ijhmt

Measuring temperature of the ice surface during its formation by using infrared instrumentation

Anatolij R. Karev, Masoud Farzaneh *, László E. Kollár

NSERC/Hydro-Quebec/UQAC Industrial Chair on Atmospheric Icing of Power Network Equipment (CIGELE) and Canada Research Chair on Engineering of Power Network Atmospheric Icing (INGIVRE), Université du Québec à Chicoutimi, 555 Boulevard de l'Université, Chicoutimi, Que., Canada G7H 2B1

Received 17 November 2005; received in revised form 15 July 2006
Available online 6 October 2006

Abstract

A non-destructive remote sensing technique was used to measure the surface temperature of a thin macroscopic water film flowing on a growing asymmetric ice accretion during its formation inside an icing research wind tunnel. Given the underlying thermodynamic conditions of this experimental series, the recorded surface temperature was always below the temperature of water fusion, $T_m = 273.15$ K, even when water shedding from growing ice accretions was observed visually. The surface temperature of ice accretions, T_s, ranged from -1 °C, for angular positions near the stagnation line, down to a certain minimum above the ambient temperature, T_a, for the greater angular positions, i.e. $T_m > T_s > T_a$.

Keywords: Non-destructive evaluation; Infrared camera; Atmospheric icing; Supercooled water film

1. Introduction

The idea of a water film flow on the surface of accreting atmospheric ice [1] enriched by the freezing fraction concept [2] has been used in atmospheric icing modeling for a long time [3]. According to this approach, the temperature of water fusion, $T_m = 273.15$ K, is taken as the reference point for the heat balance examination of a control volume of water droplets impinging on the accreting ice surface. When the calculated temperature of an ice surface is noticeably below this reference point, the impinging droplets freeze without forming a liquid film. The icing regime under such conditions is typically referred to as "dry", and the freezing fraction coefficient, defined as the fraction of the impinging droplet mass that turns into ice, is equal to unity. When the ice surface temperature approaches the reference point, the freezing fraction becomes less than unity, and a part of the unfrozen liquid is assumed to form a water film on the ice surface. This liquid film, which moves under the influence of aerodynamic and gravitational forces, can play a significant role in the heat and mass transfer processes involved. The icing regime with such a liquid film is typically referred to as "wet". Two further phenomena may occur in wet regime if unfrozen water is in excess on the ice accretion surface: first, water may be trapped into the ice lattice with subsequent spongy ice formation [4,5]; second, water may shed from the accreting ice surface [6]. In the theoretical modeling of "wet" ice growth, the temperature of the water film is assumed to be equal to water fusion temperature or close to it [3]. In fact, ice sponginess by itself is evidence that ice and water are in thermodynamic equilibrium at approximately the same temperature [7], i.e. the temperature of water fusion.

A series of experiments with artificial hailstones grown in laboratory simulations of natural conditions [8–10] confirmed that the temperature of the water film on the surface of a modeled hailstone in the wet mode is always below

* Corresponding author.
E-mail address: farzaneh@uqac.ca (M. Farzaneh).
URL: http://www.cigele.ca (M. Farzaneh).

0017-9310/$ - see front matter © 2006 Elsevier Ltd. All rights reserved.
doi:10.1016/j.ijheatmasstransfer.2006.07.015

Nomenclature

F	supercooled-water flux to an icing surface ($g\,m^{-2}\,s^{-1}$)
$\dot{h}_{i,A}\|_{V_a=20\,m\,s^{-1}}$	ice growth rate for type A nozzle and the specific value of air speed ($m\,s^{-1}$)
$\dot{h}_{i,B}\|_{V_a=20\,m\,s^{-1}}$	ice growth rate for type B nozzle and the specific value of air speed ($m\,s^{-1}$)
$\boldsymbol{n}$	normal to the ice surface
T_a	air temperature (°C)
T_m	water fusion temperature, $T_m = 273.15$ K
T_s	temperature of growing ice accretion which may include either the surface temperature of supercooled-water film or surface temperature of ice (°C)
t	time (s)
V_a	air speed ($m\,s^{-1}$)
w	liquid water content (LWC) of the two-phase flow ($kg\,m^{-3}$)

Greek symbols

α	angle with stagnation line (°)
α_C	angle between the stagnation line and the position of leading edge of either the upper or lower ice bumps (°)
α_{cam}	angle between the IR camera axis and horizontal plane; $\alpha_{cam} = 13°$
β	angle between the limiting line of the white feathers region and tangent line to the top or bottom of the icing cylinder (°)
θ	angle between the received radiation and the ice surface normal (°)
λ	thermal conductivity of substance or material ($W\,m^{-1}\,K^{-1}$)

Subscripts

a	air
c	aluminum cylinder
i	ice
s	surface
w	water

0 °C. Infrared (IR) radiometers were used in these non-destructive experiments for the evaluation of ice surface temperature. The angular temperature distribution from pole to equator was also observed, depending on the applied mode of the hailstone motion in a cloud, such as spin or nutation, and the prevailing thermodynamic conditions. Since hailstone growth in a cloud and atmospheric icing on structures in the planetary boundary layer (PBL) are very similar ice accretion processes, the question arises if the supercooling of the water film is a shared feature of these two processes. This investigation is an attempt to record supercooling at the surface of a water film flowing on the accreting ice which simulates atmospheric ice accretion. The main goal of this paper is to demonstrate that specific hailstone motion occurring inside the clouds and involving hailstone spin and nutation/precession is not the only reason for water film supercooling. Indeed, it will be shown that surface supercooling should be considered as a common feature of all ice growth processes occurring within a supercooled two-phase environment. To avoid any inadvertent influence on the modeled ice accretion process, a non-destructive remote sensing technique was used for the measurements, employing a commercial IR camera as a detector of electromagnetic waves emitted from the surfaces under investigation. A subsidiary goal of this paper is to propose improved techniques for the IR imaging of complex ice- or water-covered objects accounting for angular variation of ice and water emissivity.

2. Previous investigation in the field involving infrared instrumentation

At approximately the same time, as List's group carried out the experiments with artificial hailstones [8–10], Hansman Jr. et al. [11] investigated the effects of surface roughness on the local thermal state of ice accretions on cylinders and airfoils by using a specially designed system for global imaging, including an IR camera. It appears that, at that time, they were unaware of the results obtained in the parallel investigation by List's group and so, were unable to record any negative value for surface temperatures during the IR observation of ice accretion in the wet regime. By processing digitized color IR thermographs they were able to reveal that the wet zone near the stagnation line at "warm glaze-ice ambient temperatures" (from −0.5 °C to −4.5 °C) remained at "warm temperatures" at all times. They did not specify exact values for these temperatures, but it is obvious that they were referring to temperatures around that of water fusion. List [12] attempted to explain the recorded data by introducing the theory of non-isotropic heat transfer around the accreted object. At the same time, water film supercooling recorded at the hailstone surface was explained [13] by applying a theory [14] which was considerably different from that of simple heat balance calculation [15].

A parallel between hailstone growth and atmospheric icing processes was drawn for the first time by experimental

recording the supercooling at the surface of a water film flowing on an icing cylinder exposed to a supercooled droplet cloud [16]. IR pyrometers were used as detectors of electromagnetic waves emitted from the surface of rotating and non-rotating horizontal cylinders covered with a growing ice accretion. In both types of experiments, i.e. for rotating and non-rotating horizontal cylinders, the surface temperature of ice growing in wet mode was also found to be negative, even when the droplet shedding from the leeward side of the cylinder could be observed visually. In the case of a non-rotating icing cylinder, an angular distribution of the temperature was observed. The surface of ice growing in a wet regime near the stagnation line (i.e. for an angle formed with the stagnation line up to 30°) was always warmer as compared to the ice surface temperature from sites close to the top of the cylinder. Moreover, the angular temperature distribution around the cylinder was noticeably asymmetric with reference to the stagnation line: the top half of the cylinder was always colder than the bottom half for the same angles with stagnation line. Finally, as the experiment advanced, the angular distribution of the surface temperature became increasingly asymmetric showing a shift of the maximum value towards the bottom half of the cylinder. The IR pyrometers used in the study by Karev and Farzaneh [16] were, however, found to be hypersensitive to a number of ambient and geometrical parameters, and mainly to ambient temperature changes. The problems arising when acquiring surface temperature data using IR pyrometers implied the use of an updated sophisticated IR technique. Recently, Karev et al. [17] recorded water film supercooling during the experimental modeling of a Couette sheared water layer in plane by using an IR camera. The water film was modeled on the top surface of the ice layer prepared at the bottom of a channel. The droplet cloud was created by water dispersion from a single nozzle mounted onto the ceiling of the tunnel. Water was cooled down to 2 °C before the dispersion. The film was set flowing under the influence of air-created shear stress and was subjected to freezing from below. In this experimental attempt [17], the supercooling of the water film forming on the accreting ice surfaces was recorded as well. For the two experimental results presented therein, it was found that the value of the supercooling depends directly on the dynamic conditions modeled: the supercooling of around 2 °C was recorded for an air speed of 20 m s^{-1}, while for that of 30 m s^{-1}, the corresponding supercooling was found to be around 4 °C. Although the experimental configuration presented in [17] was of the scientific interest because of the similarity to the natural icing processes involving the flow of a water film on the planar horizontal ice surfaces, the major part of natural icing processes occurs on the structures with a complex non-planar geometry. In such a case, the water film motion on an icing surface is affected, besides the air-created shear stress, by two additional factors: gravity forces and air pressure gradient. The thermal field of a fixed circular icing structure might be a good example of the complexity of the interaction among the three factors mentioned. Further uncertainty in the experiments with planar ice accretions [17] appeared as a result of the downward dispersion of the vertically falling droplet cloud by the horizontal air cross-flow in the tunnel. In that case, the water flux reaching the horizontal icing surface could be dependent on the tunnel air speed, and the above mentioned difference in the water film supercooling recorded for various air speeds might be a consequence of varying dynamic factor, varying water flux or both factors together.

The supercooling of a water film flowing on the accreting ice surface in the experiments with artificial hailstones carried out by List's group [8–10] was reported for the defined hailstone diameter and a specific time interval, while in the experiments with non-rotating icing cylinders [16], a similar supercooling of the water film was recorded for the entire duration of the icing experiment. A final question, thus, in the context of this research is whether water film supercooling is an instant phenomenon depending on the choice of thermodynamic parameters or a permanent property of an ice accretion growing in the wet mode. A new series of experiments was, thus, designed to use an IR camera for *in situ* measurements of the surface temperatures of a water film flowing on the modeled atmospheric ice accretion of complex geometry during the entire period of the ice accretion formation.

3. Experimental setup

3.1. Experimental facilities

The ice accretions were modeled on the surface of a non-rotating horizontal cylinder exposed to a flowing supercooled droplet cloud in the CIGELE Atmospheric Icing Research Wind Tunnel (CAIRWT). This is a horizontal closed-loop low-speed icing wind tunnel 30 m in length, including a 3-m long test section whose rectangular cross-section measures 0.46 m in height and 0.92 m in width. The spray-bar system uses three nozzles located at the centreline, and 0.2 m left and right of it, respectively. A distance of 4.4 m separates the spray-bar and the mid-point of the test section where the icing structure being analyzed is usually placed. The maximum attainable air speed in the CAIRWT is around 30 m s^{-1}. A variety of ice accretion shapes may be obtained by producing dissimilar flowing droplet clouds under various controlled thermodynamic conditions.

3.2. Advantages and problems of IR instrumentation

The IR instrumentation is an excellent means for a non-destructive distant evaluation of surfacial properties of an investigated object. Readers are referred to our previous investigation [16] for an in-depth discussion of state-of-the-art of the IR surface evaluation and the presentation of both advantages and disadvantages of this method of thermal evaluation. The IR cameras were already success-

fully used for investigation of both ice [8–11,17] and water [18] surfaces. In the former case, various aspects of the ice accretion processes were under investigation, while in the latter case the processes of spreading of a thin water film were under scrutiny. Penetration depth for thermal IR radiation is very low: about ten micrometers for ice and several tens of micrometers for water, according to various authors [19,20]. The last fact facilitates obtaining temperature fields averaged over the thin surface depth, thus, the measured temperature represents a surface temperature with a great preciseness. The IR instrument used in this research was an IR camera, model SC-2000, which is manufactured by FLIR System and works in a 7–13-μm spectral range of the long wave infrared (LWIR) band. Since this wave range falls within the bracket covered by the atmospheric window, the influence of air humidity on the absorption of the IR waves could be relatively insignificant in all experiments. Therefore, a constant value of air humidity, i.e. 85%, was used in all series of experiments when adjusting image settings in the camera. A further important issue concerning any type of IR instrumentation is the calibration procedures for read-outs. Such a calibration *prior* to the measurements is unavoidable for simple types of IR instrumentation like pyrometers [16] and is carried out by comparing real temperatures, as measured by a reliable instrument such as a thermocouple, with the read-out from the IR instrument. Although formally the images in most of the IR cameras may be corrected even after recording by adjusting ambient conditions, the IR system used in this investigation was pre-calibrated for known temperature points. We refer readers to our previous study [16] for an in-depth explanation of a similar calibration procedure carried out on various objects and materials and applied to IR pyrometers. In the present research, additional calibrations were carried out with varying angles between the surface normal and the received radiation. The adjustable ambient parameters in the IR camera include: (i) local emissivity of investigated surfaces; (ii) temperature of secondary emitter; and (iii) the humidity of transmitting air. The IR images were analyzed by using commercial software, ThermCAM™ Researcher, designed to retrieve and plot any type of temperature data, representing either an instant local or averaged thermal field for some definite point, area or line. Finally, the last issue to be discussed here is emissivity of the object investigated. The IR camera allows working with both local and integral emissivity of investigated surfaces when processing IR images. Both water and ice are very good emitters over the entire detection waveband with an emissivity approaching that of a blackbody [21,22]. Moreover, IR emissivity of ice and water surfaces in the LWIR band is a function of angle with a normal to the surface investigated [23]. The problem of angular variation of the IR emissivity of ice and water surfaces in the LWIR band may be solved in a simple manner by adjustment of the local emissivity according to the angle of observation using tabulated values of emissivity for the different angles. The only problem remaining is to find precisely the incident angle for complex surfaces (see Appendix B). Furthermore, in our previous investigation [16] it was found that the read-out of IR instrument when used for measuring ice or water surface temperature is a fairly weak function of the temperature of the emitting surroundings. Similar conclusions were drawn by Horwitz [20]. The influence of the temperature of Plexiglas walls in the tunnel, which is normally kept below −7 °C throughout experiments, may thus be minimal.

3.3. Experiment design

Fig. 1 is the schematic representation of the experiment. The cylinder with a diameter of 3.8 cm is placed horizontally across the mid-height of test section and fixed into each wall of the tunnel test section. The IR camera is placed 85 cm upstream the icing cylinder in a specially designed box installed on the top of the wind tunnel. This box can be lowered in the tunnel in such a way that the angle between the camera axis and the horizontal direction is 13°, so that the entire cylinder becomes visible to the camera. To avoid influence on the air flow in the tunnel, the box usually is placed only for a few-second time interval in the tunnel and then is raised back immediately after an IR image is taken. In the inserted position, the box limits the working portion of tunnel height by 0.16 m only (see Fig. 1) and does not block the droplet cloud entirely,

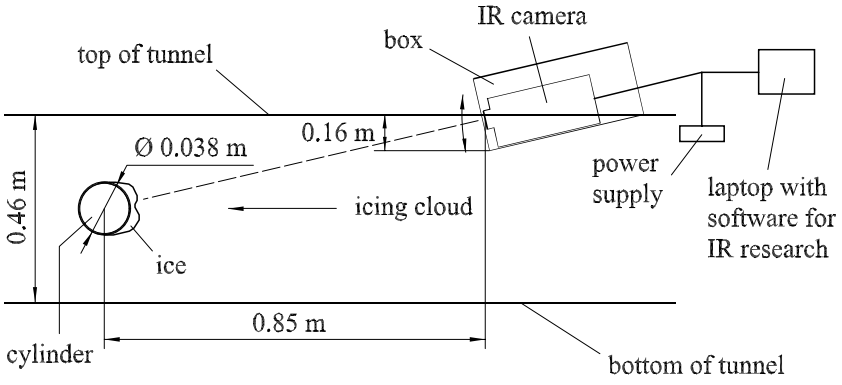

Fig. 1. Schematic view of the experimental set-up designed for infrared (IR) measurements of ice surface temperature. The figure is not to scale.

though the trajectories of some droplets near the tunnel ceiling might be deflected for several seconds. So, ice accretion goes on without interruption, even when the IR images are taken. Some additional effects on the air flow, such as levels of turbulence and blockage effect, were verified in additional experimental series and the results were found to be satisfactory. Moreover, the shapes of the ice accretions obtained under the same conditions with and without periodical insertion of the box did not show any noticeable difference. The approximate time interval between two consecutive measurements is 30–40 s. All data are recorded on the laptop by using ThermCAM™ Researcher software. A plot of temperature distribution with time at any point of an icing surface or the angular profile of local surface temperature may be obtained after processing all IR images. The experiments additionally made use of the video camera placed at grazing angle to the cylinder for recording and documenting an eventual water motion on the icing surface and shedding of droplets from it.

3.4. Choice of the thermodynamic conditions

The choice of the proper thermodynamic conditions should ensure the appearance of a water film on the surface of accreting ice. However, the so-called "warm ambient conditions", at the air temperature above −10 °C, which are most favorable for water film formation, were in fact avoided in this series of tests, taking into account their ineffectiveness in producing reliable water supercooling as compared to the instrumental error. Air temperature in the tunnel was, therefore, kept around −17 °C in all experiments, while air speed was maintained at 20 or 30 m/s. The joint effect of the modified values of the ambient temperature and LWC was verified by using the mathematical model from [3] to ensure that the amount of unfrozen water on the icing surface be approximately the same as under natural conditions. Two different types of nozzles called hereafter Types A and B nozzles were used to carry out two series of experiments in order to produce the droplet clouds with dissimilar types of droplet size distribution (DSD) and various liquid water content (LWC). We refer readers to our parallel investigation [24] where the specifics of these nozzles are scrutinized in detail. In the first series of experiments involving Type A nozzles, a droplet cloud with the median volume droplet diameter (MVD) of 43.4 μm and the mass-mean diameter (MMD) of 30.5 μm was produced. Two experiments were carried out in this series with approximately the same water flux to the icing surface F: the first involved the moderate air speed, $V_a = 20\ \mathrm{m\ s^{-1}}$, and high LWC, $w = 4.6 \times 10^{-3}\ \mathrm{kg\ m^{-3}}$, while the second was with the high air speed, $V_a = 30\ \mathrm{m\ s^{-1}}$, and moderate LWC, $w = 3 \times 10^{-3}\ \mathrm{kg\ m^{-3}}$. In the second series of experiments involving Type B nozzles, a droplet cloud with the MVD of 49.6 μm and the MMD of 25.4 μm was produced. The LWC was kept constant in both experiments from this second series, $w = 4.0 \times 10^{-3}\ \mathrm{kg\ m^{-3}}$. The only varying parameter in the experiments involving Type B nozzles was the air speed: the moderate air speed, $V_a = 20\ \mathrm{m\ s^{-1}}$, was modeled in the first experiment, while the high air speed, $V_a = 30\ \mathrm{m\ s^{-1}}$, was used in the second experiment. The presence of a water film at the surface of the accreting ice during all experiments may be verified by using the classical icing model [3]. In that way, only the air temperature was kept constant in the first experimental series consisting of two experiments with various air speeds and LWC, but with approximately the same water flux. The second experimental series involving Type B nozzles and carried out with the constant air temperature and LWC was designed in order to understand the role of the dynamic factor only, while the water flux was varying. Moreover, the two series were distinct to each other by the various DSD. The duration of experiments was set at 15 min.

4. Results and discussion

4.1. Experimental ice accretion profiles obtained by using Type A nozzles

During the experiments, ice accretions of various shapes were formed on a cylindrical surface, and the ice surface always progressed in radial direction towards the IR monitoring system. The IR system provided color pictures of the view field in the vertical plane, thus, various angular positions of the complex ice accretion surface were recorded under different observation angles. Moreover, as the ice surface advances, the angular position of any point recorded by the IR camera as the same pixel changes. In order to retrieve the temperature information from the IR pictures correctly, the observation angle for any point on the complex ice shape, though changing with time during ice accretion, should be known. The correct thermal information may, thus, be obtained if the instant ice shape and the law of changes of both ice and water emissivity with the observation angle are known. The basic features of the computation of ice and water emissivity as a function of observation angle in the present research are presented in Appendix A. In order to find out how ice accretion shapes modify with time during the icing process and evaluate the corresponding influence on the IR readouts, two experiments with durations of 5 and 15 min were carried out for each specific combination of thermodynamic conditions (totally eight experiments involving Types A and B nozzles). Two output data were collected and examined in these experiments: ice accretion profiles and ice accretion thickness. A thin preheated aluminum cutter was used to cut the ice specimens for examining the ice profiles. The information concerning ice accretion profiles were collected in two ways: by tracing the profiles manually on a cardboard and by processing the data gathered from photographs of the profiled specimens.

The ice accretion profiles obtained for time intervals of 5 and 15 min by using Type A nozzles with moderate air speed, $V_a = 20\ \mathrm{m\ s^{-1}}$, and high LWC, $w = 4.6 \times$

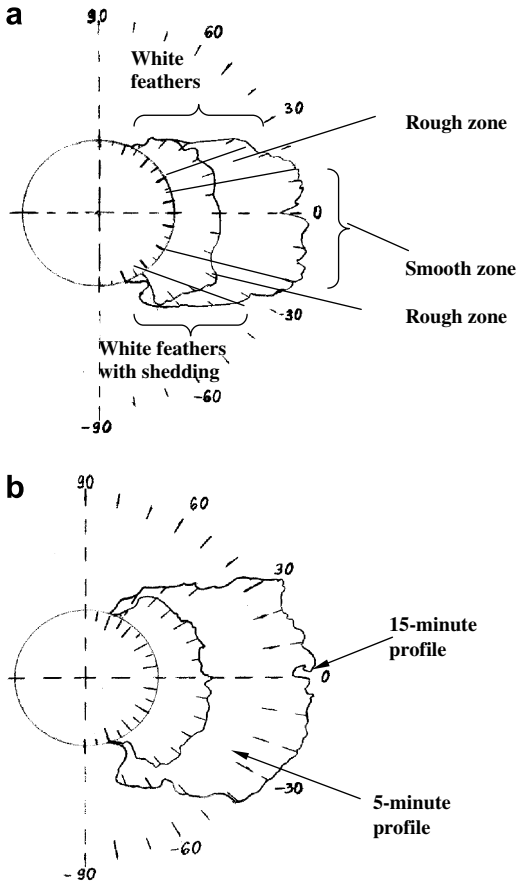

Fig. 2. Ice accretion profiles for 5- and 15-min time intervals obtained in two experiments involving Type A nozzles: (a) air speed, $V_a = 20\ \mathrm{m\ s^{-1}}$; LWC, $w = 4.6 \times 10^{-3}\ \mathrm{kg\ m^{-3}}$; and ice growth rate, $\dot{h}_{i,A}|_{V_a=20\ \mathrm{m\ s^{-1}}} = 36.7\ \mu\mathrm{m\ s^{-1}}$; (b) air speed, $V_a = 30\ \mathrm{m\ s^{-1}}$; LWC, $w = 3 \times 10^{-3}\ \mathrm{kg\ m^{-3}}$; and ice growth rate, $\dot{h}_{i,A}|_{V_a=30\ \mathrm{m\ s^{-1}}} = 45\ \mu\mathrm{m\ s^{-1}}$. Air temperature is constant for both experiments, $T_a = -17\ ^\circ\mathrm{C}$.

$10^{-3}\ \mathrm{kg\ m^{-3}}$, are presented in Fig. 2a, while corresponding profiles for the high air speed, $V_a = 30\ \mathrm{m\ s^{-1}}$, and moderate LWC, $w = 3 \times 10^{-3}\ \mathrm{kg\ m^{-3}}$ are presented in Fig. 2b. The 5-min ice accretion profile presented in Fig. 2a according to the surface state consists of three noticeably different types of zones: (i) smooth zone near the stagnation line; (ii) two rough zones of the horn-like bumps growing preferably into the air flow; and (iii) two zones of white feathers growing preferably inclined into the air flow. Thus, totally five zones are distinguished. In that way, the result of the present investigation is somehow different as compared to that presented by Hansman Jr. et al. [11]: we do not distinct transition between two first zones mentioned, while the feathers zone is selected into a separate zone. It should be mentioned that the thermodynamic conditions in the present investigation are noticeably different: LWC is significantly greater and the ambient temperature is fairly lower.

In what follows, the generalized picture of the ice accretion formation process, obtained from the experimental video recordings and post-experimental visual examinations, will be presented. Clearly, the dominant portion of the latent heat at the very beginning of any experiment is transferred by conduction to the relatively high-conductive cylinder, since $\lambda_c > \lambda_w > \lambda_i > \lambda_a$. Here λ is heat conductivity of the material, while subscripts stand: c for aluminum cylinder, w for water; i for ice; and a for air. Convective heat transfer into the flowing air which is considerably lower at this initial stage of the ice accretion formation may be, however, enhanced by the appearance of the unstable water stains with limited area. The mobile stains which appear temporarily around the stagnation line during the first 1–2 min provoke the competition between the conduction and the convective heat transfer due to additional roughness effect created. Thus, several fairly thin alternating layers of white and transparent (clear) ice form during the first 1–2 min of the ice formation process. However, for the ambient conditions with excessive liquid water flux to the icing surface, only one thin white ice layer could be revealed from the post-experimental examinations instead of the layered structure explained. The stable thin water film forming near the stagnation line after 1–2 min participates more actively in the ice accretion process, while the conductive heat transfer drops considerably due to the formation of a low-conductive ice substrate. As a result, preferably transparent ice with the smooth surface starts forming in this zone after this moment. In the two zones upward and downward the smooth ice zone, the water flux to the accreting surface is not enough for forming continuous water film. The water beds [11], which form in these zones instead, are fed upon the incoming droplets and finally, give rise to the surface roughness elements after their freezing. The roughness elements increase in number as the entire rough zone expands in both angular directions. Water shedding is initially observed at the leading edge of one of the most remote upper or lower ice bumps away from the stagnation line. Under specific thermodynamic conditions, these bumps may develop into horn-like structures. Mat or white ice is produced in rough zones, particularly at greater angular positions. Only a low number of relatively small water droplets are capable of reaching great angular locations near the top and bottom of the cylinder, around 60–70°. Due to the small size and limited concentration, they freeze immediately after the first contact with the surface forming the white ice feathers as those explained by Lozowski et al. [25]. The feathers, which possess white rime ice structure, are directed initially inside the air flow and may remain in such orientation during the entire experiment (Fig. 2a) or become inclined with the air flow after a certain time interval (Fig. 2b). As the ice accretion continues to grow, the upper and the lower rough zones become more developed causing the smooth stagnation line zone to progressively narrow. If the experimental time interval is long enough and the ambient conditions are auspicious, the latter may turn into a narrow but deep v-shaped channel (see the 15-min profile in Fig. 2a). Simultaneously, the scallop formation [26] may appear as a result of the dominant influence of roughness elements on the process of ice accretion growth. Both pairs of the profiles obtained for air speeds of $20\ \mathrm{m\ s^{-1}}$ and

30 m s^{-1} are considerably affected by the gravitational forces. As a result, the top white feathers zones are dissimilar with the bottom ones. The profiles for air speed of 20 m s^{-1} are, in particular, noticeably asymmetric, and water-shedding zone transforms into the expressed pendant formation from the 5th to the 15th minute already. The ice bumps in the rough zone considerably limit the aerial access of the water droplets to the locations with the greater angles. From time to time, however, a water flow from the bumps to the white feathers region might be observed, in particular, for an air speed of 30 m s^{-1}. In such cases, the adjoining side of the white feathers region gradually becomes soaked by flowing water, while its opposite side deflects from the direction into the flow several minutes later. Comparing the 5- and 15-min data revealed that the ice thickness changes almost linearly throughout the 15-min time interval in both experiments. Examining both pairs of profiles, the average ice growth rate in the first experiment involving Type A nozzles, $\dot{h}_{i,A}|_{V_a=20\,m\,s^{-1}} = 36.7\ \mu m\ s^{-1}$, was found to be around 20% lower than the corresponding value in the second experiment, $\dot{h}_{i,A}|_{V_a=30\,m\,s^{-1}} = 45\ \mu m\ s^{-1}$.

4.2. Ice accretion profile model

The simplified model of ice accretion growth, as shown in Fig. 3, can be used in all IR experiments in order to match surface temperature data with the experimental ice accretion profiles. Defining this model is required since the IR images are taken at 30–40 s time intervals, while the experimental ice accretion profiles are traced for 5- and 15-min time intervals only. The experimental profiles presented in Fig. 2 together with corresponding ice thickness data were used to define the model. It is assumed that the ice accretion is a crown-shaped block arc, symmetric with the stagnation line and growing into the air flow from the windward side of the cylinder. The ice surface is an arc which is concentric with the surface of the windward cylinder side in the angular domain $-\alpha_C \leqslant \alpha \leqslant \alpha_C$, while it is approximately planar in the area where $|\alpha| \geqslant |\alpha_C|$. Point C defines the position of intersection of two dissimilar ice surfaces. Angle α_C, which is defined between the stagnation line and the angular position of point C is positive when measured on the upper half of the ice accretion and negative when measured on its lower half. The absolute value of angle α_C in the model is maximal at the beginning of the experiment, $\alpha_C = 90°$, and progressively decreases during formation and growth of the ice accretion. The planar ice surface creates an angle β with the horizontal plane, which is equal to 0° for $V_a = 20$ m s^{-1} or 10° for $V_a = 30$ m s^{-1} (compare the two profiles depicted in Fig. 2a with the two profiles depicted in Fig. 2b). The ice accretion growth is simulated in the model by translating the arc-shaped surface in the radial direction inside zone $-\alpha_C \leqslant \alpha \leqslant \alpha_C$ with the velocity equal to the ice accretion growth rate recorded in either experiment, i.e. $\dot{h}_{i,A}|_{V_a=20\,m\,s^{-1}}$ or $\dot{h}_{i,A}|_{V_a=30\,m\,s^{-1}}$. Taking maximum value of angle α_C at the beginning of the experiment is, of course, a simplification in the proposed theoretical model, since any portion of ice accretions beyond the angle of $\alpha_C = \pm 70°$ was hardly observed because of insignificant local collection efficiency and absence of water flow in this zone. Furthermore, angle α_C should define the approximate angular position of the shedding process occurrence, which was never observed at any angle beyond $\alpha_C = \pm 70°$ in this experimental investigation. However, as the experiment proceeds, angle α_C decreases with time and defines the water shedding locations more precisely. Further considerable simplification in the model is an assumption concerning the smoothness of ice surfaces in all regions.

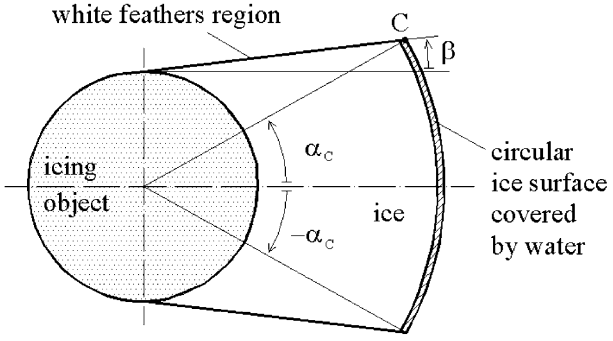

Fig. 3. Schematic representation of the ice profile model used for the presentation of the surface temperature data collected by the IR camera.

Thus, five zones experimentally observed ice accretion profiles (see Section 4.1) are divided into the three main regions in the theoretical model, mostly according to the shape and phase state of the ice surface. The arc-shaped ice surface which unites the smooth zone and the greater portions of rough zones is assumed to be covered by a water film, while the upper and lower white feathers zones together with the remaining portions of the rough zones are covered by ice of either rime or mixed structure without a surface water film. These form two lateral regions in the model. The IR system configuration in Fig. 1 makes it possible to observe only two of the three regions on the ice accretion surface modeled in Fig. 3: the upper lateral region with the planar ice surface and the greater portion of the arc-shaped ice surface. The lower lateral region is not visible in the IR camera view field.

4.3. Angular distribution of emissivity

The division of the ice surface into the regions according to surface state, as was done in the model presented in Fig. 3, simplifies the choice of either ice or water emissivity for the corresponding modeled regions. Retrieving the surface temperature data may then be defined by the variation of the emissivity with the angle between the received radiation and the surface normal only. The procedure for the calculation of this angle is presented in Appendix B. Fig. 4 presents angular variations of the ice accretion emissivity for various time sequences throughout the

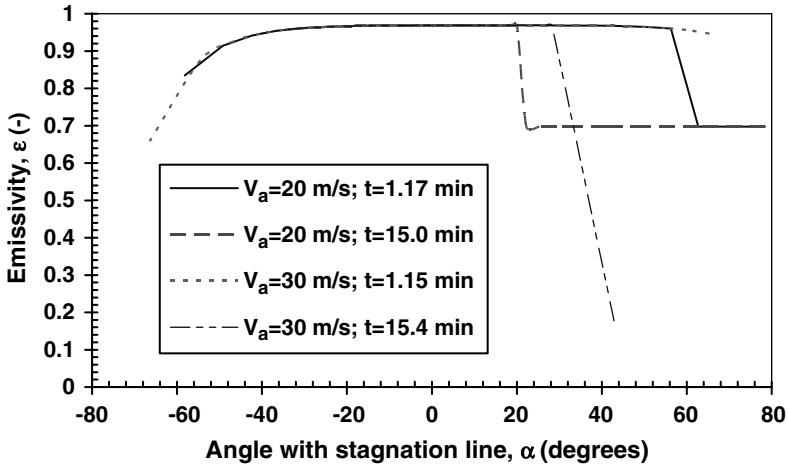

Fig. 4. Calculated emissivity of ice accretion, ε, as a function of the angle with the stagnation line for different time intervals.

experiments and for various air speeds. A small part of the upper lateral area beyond angle α_C is visible in the camera view field at the beginning of any experiment (continuous and dotted curves). Ice emissivity for the specific angle is used to retrieve the surface temperature data for this region. Water emissivity, defined as a function of the angle between direction of the received radiation and the normal to the surface is used for retrieving the surface temperature data on the remaining part of the arc-shaped surface of the ice accretion. Since the ice surface is assumed to be planar in the white feather region, the angle between the received radiation and the surface normal (θ in Fig. B1) is constant, which means that the emissivity is also constant in this region. The emissivity is significantly lower here than in the arc-shaped ice surface region because θ is great. This fact explains the abrupt change in emissivity at angle α_C as observed in Fig. 4. As the ice accretion grows, the portion of the upper lateral area beyond angle α_C, visible in the IR camera view field, increases. Thus, α_C decreases with time, with values of $\alpha_C = 21.4°$ and $\alpha_C = 28.5°$ for $V_a = 20\ \mathrm{m\ s^{-1}}$ and for $V_a = 30\ \mathrm{m\ s^{-1}}$, respectively. Although the new points are added at the bottom of the ice accretion, the angular position of any pixel with respect to the stagnation line decreases with time.

4.4. Angular distributions of surface temperature: Type A nozzles

Fig. 5a presents the angular distributions of the surface temperature for various time sequences throughout the first experiment involving Type A nozzles at air speed of $20\ \mathrm{m\ s^{-1}}$. The approximate angular position of point C with reference to the stagnation line is also presented. The bottom part of the ice accretion covered by negative angles less than $-\alpha_C$ is not visible to the camera, while α_C continuously decreases with time. So, the range from $-\alpha_C$ to α_C should shrink throughout every experiment. A few minutes after the beginning of a typical experiment, however, the ice shape, which is assumed to be symmetric in the theoretical model, starts deviating from its symmetric shape because of pendant ice formation. As a result, a small region of several degrees becomes visible at angles less than $-\alpha_C$. Therefore, several supplementary measuring points may appear for angles less than $-\alpha_C$ during that time interval. It may be concluded from the general evaluation of the distributions that the surface temperature of the ice accretion remains below the water fusion temperature of $T_m = 0\ °C$ throughout the entire experiment, even when the droplet shedding from the leeward side of the cylinder is observed visually. During the first minute of the experiment, when the heat conduction into the aluminum cylinder is still high enough, the surface temperature of the newly formed ice layer continuously raises up to $-9\ °C$ (diamonds in Fig. 5a). There was no water film observed during this stage, since all supercooled droplets froze immediately after impinging onto ice surface. The processes during this initial stage of ice formation were explained in detail in Section 4.1. The region near the stagnation line is slightly warmer than the white feathers regions, although the temperature differences between various regions are not significant. A stable thin water film is already observed near the stagnation line after 2 min (squares in Fig. 5a), and in the competition between the conduction and the convective heat transfer, the latter begins to overcome due to the additional effect of flowing water and the formation of the low-conductive ice substrate. From this moment forward, the angular distribution of surface temperature on the ice accretion becomes noticeably asymmetric with reference to the stagnation line. This distribution is fairly similar to the one observed in [16]: the surface temperature of the top half of the ice accretion is always lower than the corresponding temperature of the bottom half for the same angular positions. The region of formation of the supercooled water film is recognized here as a region with approximately constant, but negative surface temperature. The top half of the ice accretion is covered only partially by the supercooled water film, while the bottom half is covered almost entirely. The extremely

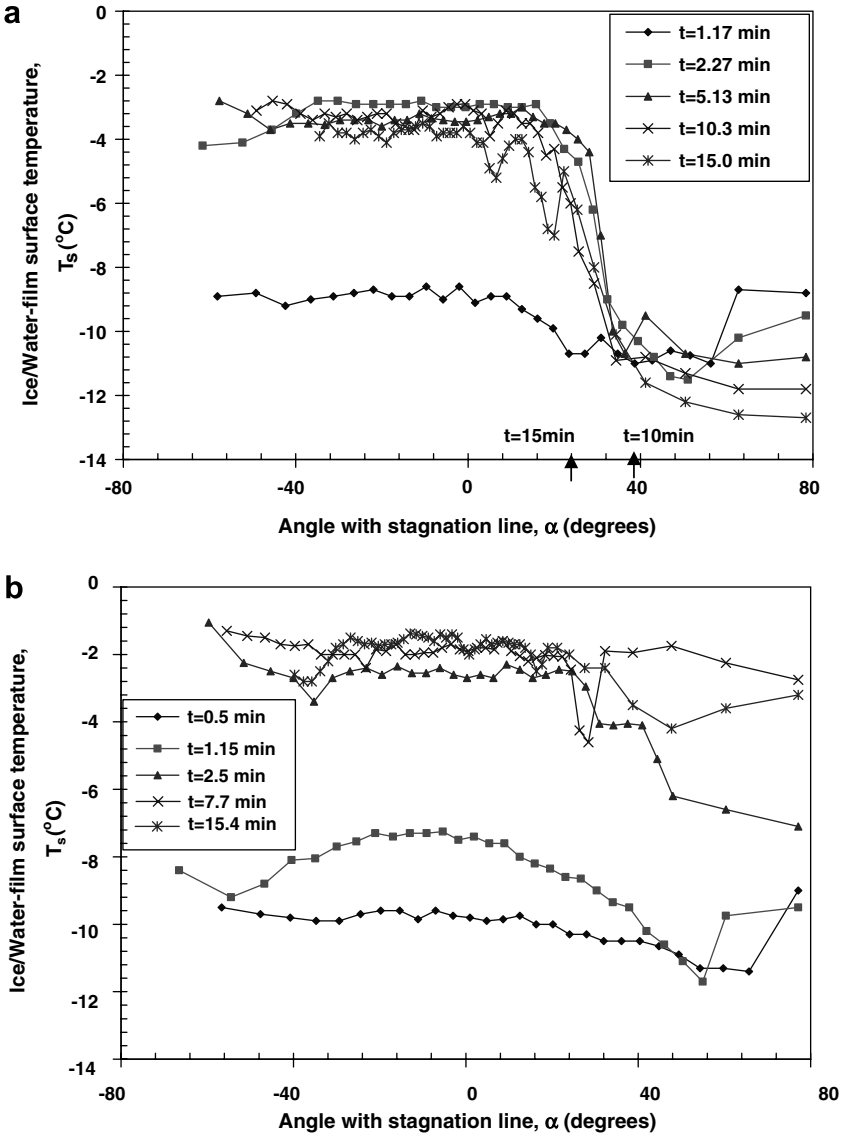

Fig. 5. Measured ice surface temperature as a function of the angle with the stagnation line for different time intervals in the experiments involving Type A nozzles. The conditions are: (a) same as in Fig. 2a; (b) same as in Fig 2b. Arrows in Fig 5a show the angular position of point C, α_C, at the time intervals indicated.

low temperatures are measured in the top white feathers zone which is very well seen in the IR camera view field for $V_a = 20$ m s^{-1} (region at the right side of the diagram). The high temperature gradient is observed between the top white feathers zone and the region of the surface water film formation during the first 5 min of the experiment. Since the first appearance of the water film, the ice surface in the white feathers zone continuously cools from −9.5 °C to ∼−13 °C while the water film surface temperature decreases gradually only 1 °C from −3 °C to −4 °C. Initial water shedding from the bottom half of the ice accretion is observed around the 6th minute of the experiment. As the rough zone at the top half of the ice accretion advances to the stagnation line, the local non-homogeneities in the surface temperature distribution become more and more pronounced, and the angular temperature gradient between the top white feathers zone and the region of the supercooled water film decreases. It remains significant, however, until the end of the experiment. Conversely, the angular gradient of the surface temperature in the region where the water film occurs is almost negligible throughout the entire experiment.

A considerably greater angular gradient of the surface temperature was observed in the second experiment, when the air speed was increased to $V_a = 30$ m s^{-1}. The angular distributions of the surface temperature for various time sequences throughout the second experiment involving Type A nozzles are presented in Fig. 5b. During the first minute of the experiment, a fairly low temperature gradient appears from the bottom to the top of the ice accretion, and is preserved throughout the entire experiment. At the end of the first minute (squares in Fig. 5b) the angular

distribution of the surface temperature shows almost symmetric shape with the stagnation line. Again, however, the maximum is observed at the bottom half of the ice accretion. The location of first appearance and evolution of the supercooled water film is almost identical to the one recorded for the previous experiment. The gradient of the surface temperature in the angular direction between the top of the ice accretion and low angular positions becomes significant after 2 min (triangles in Fig. 5b) similarly to the experiment with $V_a = 20\ m\ s^{-1}$. However, the surface temperatures at the top and bottom halves of the ice accretion equalize faster due to the higher air shear in this case. Simultaneously, the low temperature gradient in the angular direction forms where the water film covers the ice surface ($\alpha < 20°$). This temperature gradient in the surface layer of the water film remains throughout the experiment, allowing the continuous transfer of the latent heat in the angular direction. Due to partial soaking by the flowing water film, the white feathers region becomes warmer throughout the experiment, while the temperature of shedding water near the bottom approaches $-0.6\ °C$. Both angular and lateral (no figure) distributions of the surface temperature are influenced to the great degree by the appearance of the scallop formations [26] producing additional temperature oscillations in distributions, especially for $V_a = 30\ m\ s^{-1}$. It is important to mention the difference in the behavior of the surface temperature of the supercooled water film in the two experiments presented. Although the supercooled water flux to the icing surface is almost the same in both cases, the surface temperature of the supercooled water film decreases throughout the first experiment and increases throughout the second. This dissimilar behavior of the surface temperature is caused by the respectively different air speeds applied in the two cases. In the first experiment, because of the low air speed, even the formation of some roughness elements on the accreting ice surface cannot bring the air flow in the boundary layer to the turbulent state. As a result, the surface temperature remains almost the same or even decreases gradually throughout the experiment due to effect of the supercooled water droplets. In the second experiment, any formation of roughness elements in the boundary layer of the accreting ice may bring the air flow in the boundary layer at lower angular positions to the turbulent state. Development of turbulence in the flowing air accelerates the ice accretion process and increases the heat transfer from the accreting ice surface into the flowing air. As a consequence, the surface temperature of the flowing water film increases throughout the second experiment. When the transition at given angular positions is accomplished totally, the surface temperature stabilizes and stops increasing.

4.5. Experiments with Type B nozzles

The next two experiments were designed to evaluate the effect of the dynamic factor only on the surface temperature of the water film on an accreting ice surface. Also, in the third and fourth experiments, a droplet cloud with considerably modified DSD was employed (see Section 3.4). The droplet cloud created by using Type B nozzles has a greater number of larger droplets combined with noticeably smaller droplets, as compared to the droplet cloud created by Type A nozzles. The ice accretion profiles obtained for time intervals of 5 and 15 min with Type B nozzles at moderate air speed, $V_a = 20\ m\ s^{-1}$, are presented in Fig. 6a, while the corresponding profiles for high air speed,

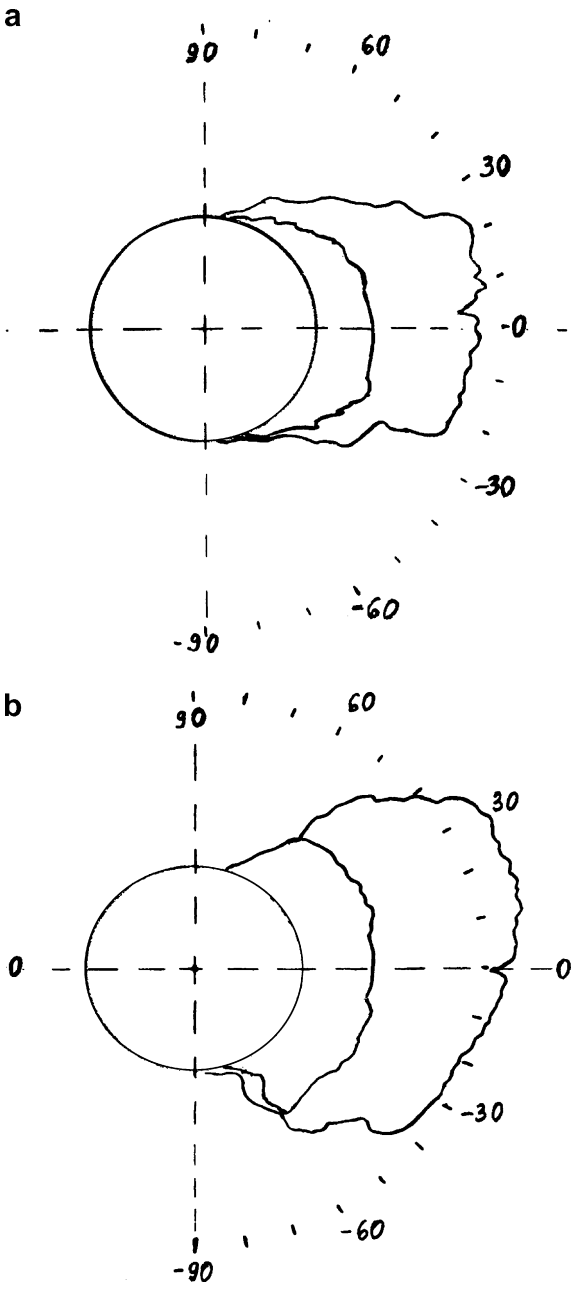

Fig. 6. Ice accretion profiles for 5- and 15-min time intervals obtained in two experiments involving Type B nozzles: (a) air speed, $V_a = 20\ m\ s^{-1}$, and LWC, $w = 4.0 \times 10^{-3}\ kg\ m^{-3}$; and ice growth rate $\dot{h}_{i,B}|_{V_a=20\ m\ s^{-1}} = 31.7\ \mu m\ s^{-1}$; (b) air speed, $V_a = 30\ m\ s^{-1}$, and LWC, $w = 4.0 \times 10^{-3}\ kg\ m^{-3}$; and ice growth rate $56.7\ \mu m\ s^{-1}$. Air temperature is constant in both experiments, $T_a = -17\ °C$.

$V_a = 30\ \mathrm{m\ s^{-1}}$, are presented in Fig. 6b. The same high LWC, $w = 4.0 \times 10^{-3}\ \mathrm{kg\ m^{-3}}$, was applied in both experiments. The 5-min ice accretion profile presented in Fig. 6a is similar to the one observed in Fig. 2a, and consists of the same three noticeably distinct zones according to the surface state: (i) smooth zone near the stagnation line; (ii) two rough zones of the horn-like bumps growing preferably into the air flow; and (iii) two zones of white feathers growing preferably inclined into the air flow. The asymmetric shape of the ice accretion is not yet pronounced in the 5-min ice accretion profile, as was observed with Type A nozzles (Fig. 2a), because the water flow on the ice surface is not entirely developed. Conversely, the 15-min ice accretion profile is asymmetric to a higher degree as compared to the corresponding 15-min ice accretion profile obtained with Type A nozzles. It should be said, however, that both pairs of profiles obtained by using Type A and B nozzles for the air speed of $V_a = 20\ \mathrm{m\ s^{-1}}$ are generally similar. In particular, angle β, defined between the preferred direction of white feathers growth and the horizontal plane could be taken 0 in both cases with a great accuracy. Examining both pairs of profiles, the average ice growth rate in the third experiment was found to be $\dot{h}_{i,B}|_{V_a=20\ \mathrm{m\ s^{-1}}} = 31.7\ \mu\mathrm{m\ s^{-1}}$.

Considerably different pairs of ice accretion profiles for the 5- and 15-min time intervals are observed for the air speed of $V_a = 30\ \mathrm{m\ s^{-1}}$, as compared to the experiments involving Type A nozzles. Both profiles from Fig. 6b are considerably asymmetric with respect to the stagnation line. The average ice growth rate in the fourth experiment was found to be higher than any rate obtained in the previous experiments $\dot{h}_{i,B}|_{V_a=30\ \mathrm{m\ s^{-1}}} = 56.7\ \mu\mathrm{m\ s^{-1}}$. To present the surface temperature data, the same model was used as that in Section 4.2. To ensure that the completely asymmetric shape of the ice accretion model was obtained in the fourth experiment, the arc-shaped zone of the ice accretion was modeled by moving the center of the imagined circle 1 cm up in the vertical plane. In this manner, the cylinder

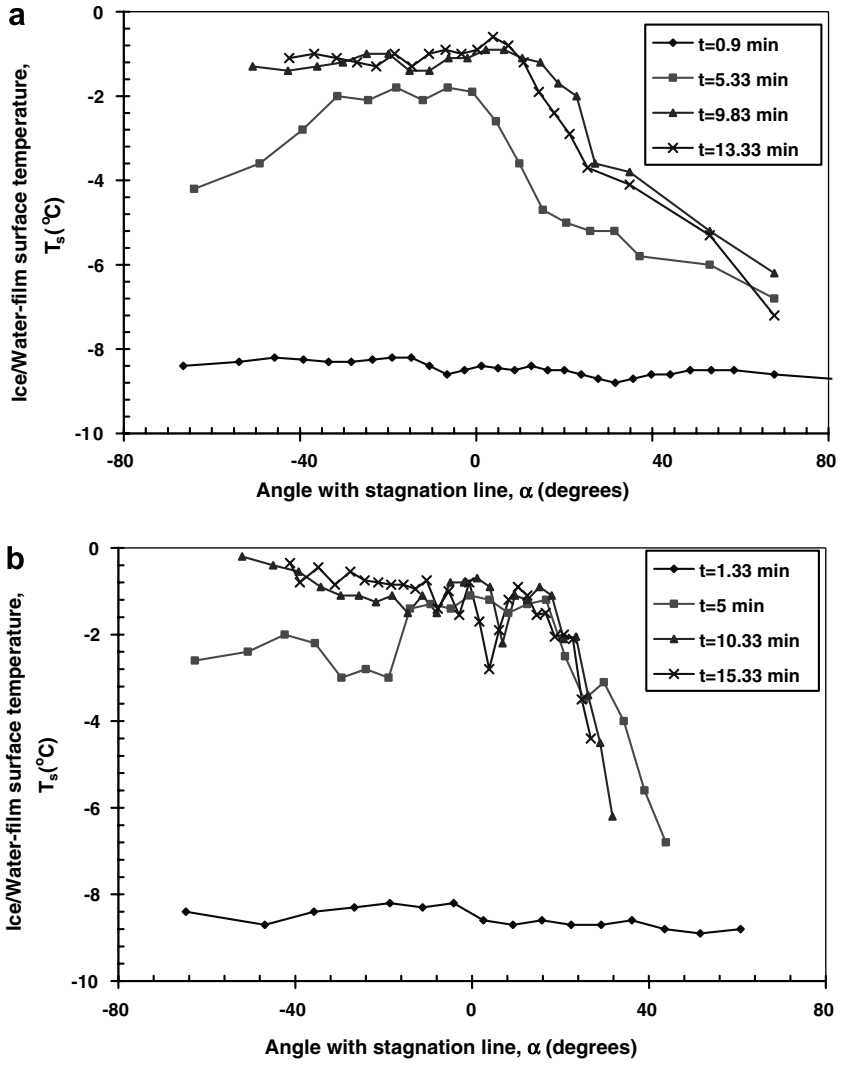

Fig. 7. Measured ice surface temperature as a function of angle with the stagnation line for different time intervals in the experiments involving Type B nozzles. The conditions are: (a) same as in Fig. 6a; (b) same as in Fig. 6b.

surface and the surface of the ice accretion could not longer be obtained by using concentric circles. Angle β, measured between the preferred direction of the white feathers growth and the horizontal plane, was found to be $\beta = 25°$, which is the largest measured in the four experiments.

A completely asymmetric distribution of the ice accretion surface temperature was obtained in both experiments involving Type B nozzles. Fig. 7a presents the angular distributions of surface temperature for various time sequences throughout the third experiment with Type B nozzles ($V_a = 20$ m s^{-1}), while Fig. 7b presents the corresponding angular distributions of the surface temperature for various time sequences throughout the fourth experiment involving same type of nozzles ($V_a = 30$ m s^{-1}). Both types of surface temperature distributions are asymmetric to a greater degree as compared to the distributions from the experiments involving Type A nozzles (compare distributions in Fig. 5a with those in Fig. 7a and distributions in Fig. 5b with those in Fig. 7b). The water film flow and water shedding are observed almost exclusively on the bottom half of the ice accretion in both cases. The difference in the surface temperature distribution may have been provoked by the different LWC in the experiments involving Type A and Type B nozzles and, particularly, by considerably different DSD in the droplet clouds. However, the oscillations in the surface temperature distributions produced by the scallop formations throughout experiments may be observed for both Type A and Type B nozzles, in particular, for the experiments with $V_a = 30$ m s^{-1}. A further similarity between the distributions in Fig. 5b and in Fig. 7b (i.e. experiments with $V_a = 30$ m s^{-1} and different types of nozzles) may be observed in the presence of a low temperature gradient at the water film surface in the angular direction. Conversely, no temperature gradient at the water film surface in the angular direction was observed for both experiments with $V_a = 20$ m s^{-1} (see Figs. 5a and 7a).

It may also be observed in Fig. 7 that the water film surface temperature increases gradually throughout both experiments involving Type B nozzles. A noticeably different development of the surface temperature in the water film throughout the first experiment with Type A nozzle (Fig. 5a) as opposed to the rest of the experiments may be accounted only for the extreme combination of low air speed and high LWC in that case ($V_a = 20$ m s^{-1}; $w = 4.6 \times 10^{-3}$ kg m^{-3}).

5. Conclusions

In summary, the following principal conclusions may be drawn from this research:

1. Ice accretion surface temperatures were found to be negative throughout all experiments in this investigation, even when droplet shedding was observed visually from the leeward side of the ice accretion. This study indicates that atmospheric icing and hailstone growth phenomena, despite their dissimilarities, may have a common feature, which is water film supercooling on the accreting ice surface.
2. The temperature of the water film recorded on the surface of the ice accretions in the experiments may decrease or increase gradually throughout the experiments, but never reaches the temperature of water fusion. *Thus, these experimental series confirm that the supercooling of a macroscopic water film appearing on the accreting ice surfaces is rather a permanent than an instant property of ice accretion processes.*
3. The angular temperature distribution around accreting ice surfaces is noticeably asymmetric with reference to the stagnation line. As a result of gravity, the top half of the accretion is always colder than the bottom half for the same angles with a stagnation line which is consistent with the findings obtained in our previous research [16]. The angular temperature gradient on the surface of the water film may disappear very frequently throughout the experiments.
4. Finally, supercooling of a water film flowing on the accreting ice surface may have wide applicability to crystallization problems in closely related fields.

The dynamics of the water film flowing on an icing surface requires a new description of the water supercooling mechanism. To date, only one approach [27,28], based on the idea and theoretical considerations from [14], satisfies these requirements. This approach, with certain modifications, should be tested in future experimental investigations.

Acknowledgements

This study was carried out within the framework of the NSERC/Hydro-Quebec Industrial Chair on Atmospheric Icing of Power Network Equipment (CIGELE) and the Canada Research Chair on Atmospheric Icing Engineering of Power Network (INGIVRE) at the Université du Québec à Chicoutimi. The authors would like to thank all CIGELE sponsors for their financial support. The authors would like also to acknowledge Mr. Pierre Camirand for his technical support and Mr. S. Vaslon (graduate student at CIGELE) for help with acquisition of IR data.

Appendix A. Emissivity calculation of ice and water surfaces for varying angles

According to Rees and James [23] who adapted a simple Fresnel model for the examined surface, the variations of the emissivity of either ice or water, ε, as a function of the angle θ between the received radiation and the surface normal may be determined as follows:

$$\varepsilon = 1 - \frac{1}{2}\frac{[(n^2 - \sin^2\theta)^{1/2} - \cos\theta]^2}{[(n^2 - \sin^2\theta)^{1/2} + \cos\theta]^2} - \frac{1}{2}\frac{[n^2\cos\theta - (n^2 - \sin^2\theta)^{1/2}]^2}{[n^2\cos\theta + (n^2 - \sin^2\theta)^{1/2}]^2} \quad (A.1)$$

where n is the refractive index, in which only the real part is preserved, while the imaginary part is neglected. For water $n = 1.43 \pm 0.03$, while for ice $n = 1.60 \pm 0.09$ should be taken. At $\theta = 0°$, the model provides the values $\varepsilon = 0.969$ for water and $\varepsilon = 0.947$ for ice, which are in the satisfactory consistence with the integral values of water and ice emissivity within the region of the atmospheric window in the LWIR band [21–23]. The surfaces of both materials are assumed to be homogeneous and planar. The model, however, fails to predict the natural values of emissivity for angles greater than 70°, since the assumption for a zero value for the imaginary part of the refractive index is no longer valid. Moreover, the natural roughness of ice surfaces and roughness of the moving water surface created by surface waves are two factors decreasing effectiveness of this model.

Appendix B. Determination of angle between the received radiation and the surface normal

Fig. B1 presents schematically the relationship between the various angles: $\alpha_{cam} = 13°$ is the angle between the plane of IR camera view field and vertical plane; θ is the angle between the received radiation and the surface normal, **n**; and $\alpha_{i,t}$ is angular position of the ith pixel relatively to stagnation line at time t. Since the IR camera axis is inclined with the horizontal direction at an angle α_{cam}, the plane of the camera view field creates the same angle α_{cam} with the vertical plane. The projection of the horizontal cylinder on the plane of the camera view field is a rectangle whose height represents the angular variations of the surface temperature, while its length represents the corresponding axial variations of the surface temperature. A standard IR system with a built-in 24° lens allows for evaluating the angular temperature variations by using 29 pixels, which are denoted by the index i in Fig. B1. The pixels carry information about the temperature of the 29 differential areas on the cylinder surface arranged in the angular direction from the top of the cylinder to its bottom. The distance between the IR camera and the cylinder is considerably longer than the cylinder diameter, thus, it is assumed that the rays of received radiation from the first angular area, $i = 1$, and last angular area, $i = 29$, are parallel. The first angular area is always observed on the leeward side of the cylinder at the angle of $90° + \alpha_{cam} = 103°$ relatively to the stagnation line and thus, does not contain any information about the surface temperature of the ice accretion forming on the forward portion of the cylinder. The 29th and last angular area is observed at the beginning of the experiment on the forward portion of the cylinder at an angle of $-90° + \alpha_{cam} = -77°$. As ice accumulation grows on the cylinder, the same ith pixel in the camera view field gives information from the lower angular area relatively to the stagnation line (check how α_{i,t_0} transforms into $\alpha_{i,t}$). Moreover, as a result of the appearance and growth of ice accretion on the cylinder, j supplementary pixels are added at every time step at the bottom of the rectangle representing projection of the horizontal cylinder on the plane of the view field of the camera. The number of supplementary pixels is determined by the instant ice accumulation thickness.

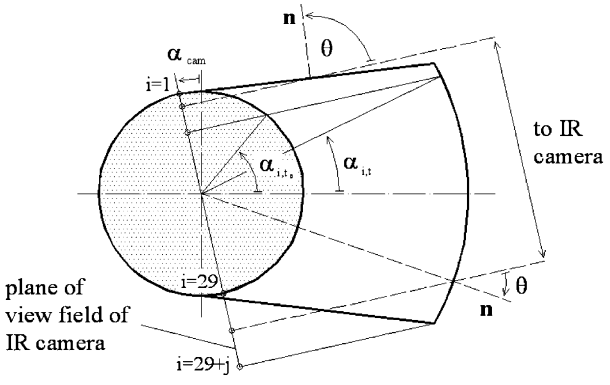

Fig. B1. Schematic representation of the ice profiles as they are seen in the plane of IR camera view field.

The angle $\alpha_{i,t}$ may be defined from geometrical configuration, if the ice growth rate $\dot{h}_i$ is known. Furthermore, the angle β which was defined as the angle between the preferred direction of growth of the white feathers and the horizontal plane is determined by type of the ice accretion. If the angles α_{cam}, β and $\alpha_{i,t}$ are known, the angle between the received radiation and the surface normal, θ, may be easily found. In the white feather regions, it is determined as follows:

$$\theta = \frac{\pi}{2} + \beta - \alpha_{cam} \quad (B.1)$$

In arc-shaped ice surface region when the bare cylinder surface is observed, angle θ is determined as follows:

$$\theta = |\alpha_{i,t} - \alpha_{cam}| \quad (B.2)$$

As may be noted, angle θ does not depend on $\alpha_{i,t}$ in the region of white feathers, since the ice surface is assumed to be straight here. Conversely, in the region of arc-shaped ice surface it does not depend on angle β.

References

[1] T.E.W. Schumann, The theory of hailstone formation, Q. J. Roy. Meteorol. Soc. 64 (1938) 3–21.
[2] B.L. Messinger, Equilibrium temperature of an unheated icing surface as a function of air speed, J. Aerospace Sci. 20 (1953) 29–42.
[3] E.P. Lozowski, J.R. Stallabrass, P.F. Hearty, The icing of an unheated, non-rotating cylinder. Part I: A simulation model, J. Clim. Appl. Meteorol. 22 (1983) 2053–2062.
[4] D. Fraser, C.K. Rush, D. Baxter, Thermodynamic Limitations of Ice Accretion Instruments, National Aeronautical Establishment Canada, Laboratory Report LR-32, 1952.

[5] R. List, Wachstum von Eis-Wassergemischen im Hagelversuchskanal, Helv. Phys. Acta 32 (1959) 293–296.
[6] J.N. Carras, W.C. Macklin, The shedding of accreted water during hailstone growth, Q. J. Roy. Meteorol. Soc. 99 (1973) 639–648.
[7] L. Makkonen, Salinity and growth rate of ice formed by sea spray, Cold Reg. Sci. Technol. 14 (1987) 163–171.
[8] R. List, F. Garcia-Garcia, R. Kuhn, B. Greenan, The supercooling of surface water skins of spherical and spheroidal hailstones, Atmos. Res. 24 (1989) 83–87.
[9] F. Garsia-Garsia, R. List, Laboratory measurements and parametrizations of supercooled water skin temperatures and bulk properties of gyrating hailstones, J. Atmos. Sci. 49 (1992) 2058–2073.
[10] B.J.W. Greenan, R. List, Experimental closure of the heat and mass transfer theory of spheroidal hailstones, J. Atmos. Sci. 52 (1995) 3797–3815.
[11] R.J. Hansman Jr., K. Yamaguchi, B. Berkowitz, M. Potapczuk, Modeling of surface roughness effects on glaze ice accretion, J. Thermophys. 5 (1991) 54–60.
[12] R. List, Physics of supercooling of thin water skins covering gyrating and hailstones, J. Atmos. Sci. 47 (1990) 1919–1925.
[13] A. Karev, Thermodynamic and radar properties of water skin on the surface of growing hailstones, Russ. Meteorol. Hydrol. (2) (1993) 37–43.
[14] L.G. Kachurin, On aircraft icing theory, Izvestiya Akademii Nauk SSSR, Geophys. Ser. 6 (1962) 823–832.
[15] F.H. Ludlam, The hail problem, Nibula 1 (1958) 12–96.
[16] A.R. Karev, M. Farzaneh, Infrared laboratory measurement of ice surface temperatures during experimental studies on the formation of ice accretion, in: Proceedings of the 13th Conference of International Society of Offshore and Polar Engineering (ISOPE), Honolulu, Hawaii, USA, 25–30 May 2003, vol. 1, pp. 390–397.
[17] A.R. Karev, M. Farzaneh, L.E. Kollár, S. Vaslon, Freezing of flowing water in an open channel under supercooled conditions: preliminary results, in: Proceedings of the 17th IAHR International Symposium on Ice, Saint-Petersburg, Russia, 21–25 June 2004, vol. 1, pp. 379–384.
[18] J.R. Saylor, G.B. Smith, K.A. Flack, Infrared imaging of the surface temperature field of water during film spreading, Phys. Fluids 12 (2000) 597–602.
[19] J.E. McDonald, Absoption of atmospheric radiation by water films and water clouds, J. Meteorol. 17 (1960) 232–238.
[20] J.W. Horwitz, Water at the ice point: a useful quasi-blackbody infrared calibration source, Appl. Opt. 38 (1999) 4053–4057.
[21] W.M. Irvine, J.B. Pollack, Infrared optical properties of water and ice spheres, Icarus 8 (1968) 324–360.
[22] J.W. Schaaf, D. Williams, Optical constants of ice in the infrared, J. Opt. Soc. Am. 63 (1973) 726–732.
[23] W.G. Rees, S.P. James, Angular variation of the infrared emissivity of ice and water surfaces, Int. J. Remote Sens. 13 (1992) 2873–2886.
[24] L.E. Kollár, M. Farzaneh, A.R. Karev, Modeling droplet-size distribution near a nozzle outlet in an icing wind tunnel, Atomization and Sprays 16 (2006) 673–686.
[25] E.P. Lozowski, J.R. Stallabrass, P.F. Hearty, The icing of an unheated, nonrotating cylinder. Part II: Icing wind tunnel experiments, J. Clim. Appl. Meteorol. 22 (1983) 2063–2074.
[26] M. Vargas, J.A. Giriunas, T.P. Ratvasky, Ice accretion formation on a NACA 0012 swept wind tip in natural icing conditions, AIAA paper 2002-0244.
[27] A.R. Karev, M. Farzaneh, E.P. Lozowski, Character and stability of a wind-driven supercooled water film on an icing surface – I. Laminar heat transfer, Int. J. Thermal Sci. 42 (2003) 481–498.
[28] A.R. Karev, M. Farzaneh, E.P. Lozowski, Character and stability of a wind-driven supercooled water film on an icing surface – II. Transition and turbulent heat transfer, Int. J. Thermal Sci. 42 (2003) 499–511.